AIAA SciTech Forum
5-9 January 2015, Kissimmee, Florida
23rd AIAA/AHS Adaptive Structures Conference

10.2514/6.2015-0788

A Bi-Stable Mechanism for Blade Span Extension in Rotary-Wing Micro Aerial Vehicles

Matthew P. Misiorowski[1] Farhan Gandhi[2]

Rotorcraft, Adaptive and Morphing Structures (RAMS) Lab
Department of Mechanical, Aerospace and Nuclear Engineering
Rensselaer Polytechnic Institute, Troy, NY 12180

Michael Pontecorvo[3]

Advanced Concepts, Sikorsky Aircraft Corporation, 6900 Main St, Stratford, CT 06614

Previous studies have shown that rotary-wing micro air vehicles have limited range and endurance due to the high power loading associated with small rotors. A span morphing rotor could provide performance improvements associated with a larger rotor diameter while maintaining the small vehicle footprint in constrained environments. This paper presents a concept where increase in centrifugal force with increasing rotor RPM causes snap-through of a bi-stable mechanism within the blade, resulting in rotor span extension. The design and analysis of such a system is presented and initial rotor tests showed asynchronous extension of the two blades due to dissimilarity. A cable-pulley mechanism was designed and integrated into the prototype to ensure synchronous extension of the two blades. Using high-speed camera footage for measurement of rotor span extension and RPM, the prototype rotor was observed to snap-through at about 950 RPM, over about ¼ rotor revolution (0.015 sec). The snap-through RPM calculated from the high-speed camera was verified using data from a Hall Effect sensor on the rotor hub. Model simulation results of rotor extension versus RPM showed excellent correlation with measurement.

I. Introduction

Hover-capable Micro Aerial Vehicles (MAVs) potentially offer the soldier tremendously improved situational awareness in zones of conflict. However, they are limited by low endurance, range and payload capability. One approach to improving these attributes is through improving the rotor aerodynamic efficiency. The small rotors operating at low Reynolds numbers are known to have a significantly lower Figure of Merit compared to rotors on larger helicopters operating at much higher Reynolds numbers (Refs. 1–5). The rotary-wing MAVs being considered by the US Army for the applications discussed above have a rotor diameter nominally of around 6-9 inches. The small size allows the MAV to maneuver in confined spaces and to be easily stored in the soldier's pack. However, the MAV may not always face the most stringent space constraints during operation. A span-morphing rotor whose diameter can increase when flying in less confined spaces, will operate at a much reduced disk loading, which would in turn significantly improve Power Loading, Figure of Merit and endurance/range/payload capability. While span-extension morphing has been previously considered for large rotors (Refs. 6–9), rotary-wing MAVs have not yet exploited this concept. The key lies in the simple (low-weight, preferably passive) implementation of concept.

The present study focuses on centrifugally enabled micro-rotor span extension based on the use of a bi-stable mechanism. While centrifugally enabled span morphing has previously been considered for large rotors (Ref. 8), coupling with bi-stability has not been previously examined. Bi-stable structures are of interest for morphing applications because they allow a large morphing stroke and do not require a locking mechanism in either configuration since they correspond to stable equilibrium states (Ref. 10). Examples of bi-stable structures for aerospace morphing applications include the work by Weaver et al., (Ref. 11) and Schultz (Ref. 12) on fixed-wing applications, and by Gandhi et al. (Refs. 13-15) on helicopter rotor chord extension morphing. The study in Ref. 15 is particularly relevant as chord extension due to the snap-through of bi-stable elements is centrifugally enabled.

[1] Ph.D. Student, AIAA Student Member.
[2] Rosalind and John J. Redfern Jr. '33 Professor of Aerospace Engineering, AIAA Associate Fellow.
[3] Senior Engineer, Advanced Concepts, AIAA Member.

The following sections describe the design, analysis and fabrication of the mechanism of a variable-span micro-rotor in which increase in centrifugal force with increase in RPM produces snap-through of a bi-stable element and results in span extension. Designed for a two-bladed rotor, a system is developed to synchronize the deployment on both blades to prevent imbalance problems associated with one blade deploying first. The prototype is tested on a hover stand, span extension with increase in RPM is experimentally demonstrated, and analysis results are validated against test.

II. Concept and Analytical Model

The bi-stable mechanism on which rotor blade span extension in the present study is based is the von-Mises truss (VMT), a mechanical system first introduced in 1923 (Ref. 16) to model the stability of a shallow arch. As indicated in Fig. 1a, it consists of two pinned-pinned rigid members whose independent ends slide laterally against a spring restraint when a force is applied to the vertex to transition the VMT from one stable equilibrium condition to the other. Alternatively, variable length links may be used with the restraining springs contained within these links, as indicated in Fig. 1b. This arrangement is particularly useful if motion in the lateral direction is not permissible. Figure 2 (from Ref. 15) shows the implementation of a rotor chord extension morphing system using a VMT. The vertex of the VMT connects to a plate that can retract within the chord of the blade or extend to increase the effective chord length. Such a system, if rotated 90 deg, could be adapted to produce span extension.

To realize span extension in the present study, two changes are introduced to the conceptual design in Ref. 15 in addition to the 90 deg rotation. As indicated in the schematic sketch in Fig. 3, the bi-stable mechanism uses only one-half of the VMT shown in Figs. 1 and 2, or a single link of the truss. Additionally, a variable length link with an internal spring is used. One end is pivoted as indicated in the figure and the other end constrained so motion is purely along the spanwise direction, and the span extension mechanism operates between two parallel tracks.

In Fig. 3 when the bi-stable mechanism is in the first equilibrium state, the uncompressed link length is L_o, and its pinned end forms the angle θ_o. The free end of the link that slides in the spanwise direction is connected to an insert that is contained within the inner fixed section. As the centrifugal force on the insert increases, the link compresses, its free end begins to slide along the spanwise direction (displacement variable, x, is shown on Fig. 3). After going through the unstable equilibrium condition where the link has maximum compression, the link begins to expand again. If the force at the free end is removed, the bi-stable mechanism would settle in its second equilibrium state. In a micro-rotor the centrifugal force persists during operation, and a mechanical stop prevents further extension of the mechanism beyond the geometry corresponding to the second equilibrium state. The stiffness of the compression spring within the variable length link is denoted by k, and the mass of the insert attached to the free end of the link is m.

The equation of motion governing this bi-stable system is derived using Lagrange's equation, as described below.

$$\frac{\partial}{\partial t}\left(\frac{\partial \mathrm{L}}{\partial \dot{x}}\right) - \frac{\partial \mathrm{L}}{\partial x} = F \qquad [1]$$

$$L = T - V \qquad [2]$$

Kinetic energy of the system $$T = \frac{1}{2} m \dot{x}^2 \qquad [3]$$

Potential energy of the system $$V = \frac{1}{2} k (\Delta L)^2 = k \left[L_0 - \frac{L_0 cos(\theta_0)}{cos\left(tan^{-1}\left(\frac{L_0 sin(\theta_0) - x}{L_0 cos(\theta_0)} \right) \right)} \right]^2 \qquad [4]$$

$$\frac{\partial}{\partial t}\left(\frac{\partial \mathrm{L}}{\partial \dot{x}}\right) = m\ddot{x} \qquad [5]$$

$$\frac{\partial \mathrm{L}}{\partial x} = k\left(x - L_0 sin(\theta_0)\right) - \frac{k\left(x - L_0 sin(\theta_0)\right)}{cos(\theta_0)\sqrt{\frac{\left(x - L_0 sin(\theta_0)\right)^2}{\left(L_0 cos(\theta_0)\right)^2} + 1}} \qquad [6]$$

$$m\ddot{x} + k\left(x - L_0 sin(\theta_0)\right) - \frac{k\left(x - L_0 sin(\theta_0)\right)}{cos(\theta_0)\sqrt{\frac{\left(x - L_0 sin(\theta_0)\right)^2}{\left(L_0 cos(\theta_0)\right)^2} + 1}} = F \quad [7]$$

In Eq. 7, *F* represents the centrifugal force (CF), and its mathematical representation is provided in section III.

III. Prototype Design and Fabrication

A prototype is designed to demonstrate the bi-stable mechanism described in the previous section transitioning under centrifugal load and resulting in span extension. The present study is focused on the operation of the mechanism, and not the aerodynamic behavior of a variable span rotor. Consequently, a simplified system is designed and fabricated with all the functional components, but without aerodynamic profiles. Instead of designing a variable span rotor blade, per se, the bi-stable mechanisms are contained in an aluminum C-channel, and the inserts representing the extending portions of the blades slide within this channel.

Figure 4 shows one half of the channel on one side of the rotor hub, with the bi-stable mechanism and the attached insert in the compact as well as the extended span configurations. Based on the parameters shown in the figure (offsets δ_1 and δ_2, uncompressed link length, L_o, corresponding angle, θ_o, insert length of L_e, and an overlap length of βL_e in the extended configuration), the radius in the compact configuration can be expressed as:

$$R_c = \delta_1 + L_0 sin\theta_0 + \delta_2 + L_e = \delta_1 + 3L_0 sin\theta_0 + \delta_2 + \beta L_e \quad [8]$$

From the above, the increase in span can be shown to be mathematically equal to the "stroke length" of the bi-stable device.

$$\text{Span extension} = (1-\beta)L_e = 2L_0 sin\theta_0 = \text{bi-stable mechanism stroke length} \quad [9]$$

And the radius in the extended configuration is:

$$R_e = R_c + (1-\beta)L_e \quad [10]$$

Based on the capability of the in-house micro-rotor test facility, the value of R_c was selected to be 139 and the value of R_e was 197 mm (a 40% increase), with an overlap parameter of $\beta = 0.1$, in the extended configuration. From Eq. 9 it appears that the span extension can be maximized by increasing $L_0 sin\theta_0$. However, there are practical limits that constrain the maximum extension that can be achieved using a single bi-stable mechanism of the type shown in Figs. 3 and 4. Consider, for example, the case in Fig. 5a where a large stroke length is desired but the width of the channel is relatively small (corresponding to realistic blade aspect ratios). The minimum link length during transition is $L_0 cos\theta_0$ and the compression ratio of the internal spring would be greater than $L_0(1 - cos\theta_0)$. However, springs with significant stiffness generally have limits on maximum achievable compression ratios. Alternatively, Fig. 5b shows a schematic where the same stroke (as in Fig. 5a) is realized using a smaller link angle, θ_0, but a larger link length, L_0. While the required reduction in link length and internal spring compression are smaller, the channel width becomes too large with negative implications on blade aspect ratio (resulting in a very stubby blade). The link initial angle, θ_0, as well as the spring stiffness, *k*, also have a strong impact on the force required to transition the mechanism from the "retracted" to "extended" states. For a specific mass, *m*, of the insert, this determines the rotational speed at which the mechanism deploys.

Reasonable initial approximations are made on the mass of the insert, and deployment is targeted at just a little over 750 RPM (the switch-on RPM of the motor). This was done to avoid the excessive vibration and potential safety issues in the test associated with high RPM deployment. The analytical model in Section II is used to predict the span extension as a function of RPM, with the centrifugal force in Eq. 11 defined as:

$$CF = m \cdot (x_{cm} + x) \cdot \Omega^2 \quad [11]$$

Here x_{cm} is an offset along the insert where the center of mass is located.

An iterative procedure is used to select parameters such as channel width, the offsets, and spring stiffness, while considering constraints such as those discussed above as well as availability of commercial off-the-shelf components such as compression springs. The system parameters from the design process are listed in Table 1.

Table 1: Rotor dimensions and component characteristics used to describe contracted and extended radius as well as centrifugal force acting on inserts.

Extended Radius (R_e)	197 mm
Retracted Radius (R_r)	139 mm
Chord Length	45 mm
θ_0	40°
L_0	44.5 mm
δ_1	16 mm
δ_2	30 mm
L_e	64 mm
$\beta \cdot L_e$	6.4 mm
Spring Stiffness (k)	4.92 N/mm
Blade Mass	0.019 kg
Spanwise Location of CG (x_{cm})	78.7 mm

Based on the specified design, a micro-scale span morphing prototype, pictured in Fig. 6 was fabricated. The system uses a rigid aluminum C-channel, which spins about the central large-diameter bolt, with extendable Delrin inserts attached to variable length links. One end of each link is pinned to the C-channel, and the other is pinned to the Delrin insert. Housed within the variable length links are compression springs responsible for the bi-stability of the mechanism. Although this system cannot generate lift due to the absence of an aerodynamic outer profile, it is adequate to demonstrate span extension achieved through the transition of the bi-stable mechanism due to the centrifugal force acting on the Delrin inserts.

An important design feature of the prototype rotor is the slot that is cut in each of the Delrin inserts, which allows the insert to slide around a pin that is grounded to the c-channel. Contact between the end of the slot and the pin in the fully extended state provides a mechanical stop that prevents the insert from extending past the second stable equilibrium position of the bi-stable mechanism.

IV. Experimental Procedure

Centrifugally enabled span extension in conjunction with the bi-stable mechanism is demonstrated experimentally on the micro-rotor test facility at Rensselaer Polytechnic Institute's Rotorcraft, Adaptive and Morphing Structures (RAMS) Lab. The rotor test stand is powered by a Rimfire 1.20 450 kV electric motor that has been geared down by a ratio of 4:1 using a planetary gearbox (Fig. 7). The prototype is rigidly attached to the output shaft of the gearbox within which is embedded a permanent magnet. The RPM of the rotor is measured by a Hall Effect sensor which detects each rotation of the magnet, and is calculated using a NI USB-6212 data acquisition system. A Phantom V4.3 high speed camera is used to visually detect the occurrence of snap-through, verify the RPM measurements and measure the prototype extension. The high-speed camera software allows stepping through individual frames, and Fig. 8 shows how extension measurements are made by determining the position of the insert in successive frames. The high-speed camera is operated, nominally, at 1000 frames/sec. At a rotational speed of 1000 RPM, the camera would therefore record 60 images over one rotor revolution (at lower rotational speeds of around 900 RPM where snap-through occurs, the number of frames per revolution is even greater).

While the high-speed camera images are excellent for measurement of prototype extension, and the frames can be used to calculate rotor RPM, the Hall Effect sensor provides real-time RPM measurements as well as an indication of snap-through during the test. When snap-through occurs and the prototype very quickly extends, the rapid increase in rotor radius results in a significantly higher rotor rotational moment of inertia. The rotor is observed to momentarily lose speed (as indicated by the Hall Effect sensor and verified by the measurements of the high speed camera). However, the rotor stand is equipped with an RPM governor, and after the initial drop in RPM to conserve momentum, the governor restores RPM to the rate prior to snap-through.

In addition to the procedures described above with regards to the rotor stand experiments, the bi-stable mechanism was tested in an Instron model 4204 material testing machine with a 1 kN load transducer to verify the friction coefficients on the prototype.

V. Friction Measurements, First Rotor Test, and Model Refinement

The bi-stable mechanisms on each half of the channel were tested in the Instron machine under input displacement conditions. In the absence of any friction, the predicted force is symmetric about zero, as shown in Fig. 9. The predicted force is obtained by solving Eq. 7 quasi-statically for *F*, for a prescribed input, *x*. The measured curves for both the bi-stable mechanisms show a higher critical force required for transition to the second equilibrium position, effectively an upward offset of the force/displacement curve. This is attributed primarily to friction. It can be observed in Fig. 9 that the critical force (snap-through force) differs somewhat for the two mechanisms on either side of the channel.

Removing the internal spring from the variable length link, the friction coefficient is measured using an "incline test" (the inclination of the C-channel relative to horizontal is increased incrementally, and the angle at which the insert begins to slide is determined). This is done for both inserts, and the test is repeated several times for each insert and averaged. The experimentally measured friction coefficient values are determined to be 0.254 and 0.372 respectively. It should be noted that these measurements "bundle" friction between the Delrin insert and the Aluminum channel, as well as friction in the variable length link (which also involves Delrin sliding against Aluminum), and at the pin-joints.

The friction force is introduced into the quasi-static governing equation for the bi-stable mechanism, as shown.

$$k\left(x - L_0 sin(\theta_0)\right) - \frac{k\left(x - L_0 sin(\theta_0)\right)}{cos(\theta_0)\sqrt{\frac{\left(x - L_0 sin(\theta_0)\right)^2}{\left(L_0 cos(\theta_0)\right)^2} + 1}} = F - F_{FR} \quad [12]$$

$$\text{where } F_{FR} = \mu N \quad [13]$$

Using the experimentally derived values of friction coefficient, μ, the simulated force versus displacement curves are shown on Fig. 9. The normal force, N, in the simulation comes from the component in the force in the compression spring in the variable length link acting normal to the span, and is calculated as

$$N = k\Delta L \cos(\theta_0 - \theta) \quad [14]$$

A comparison of the simulated curves in Fig. 9 with the experimental data from the Instron test shows excellent correlation of the critical snap-through force, and of the overall behavior prior to the mechanism passing the unstable equilibrium position. Thereafter, the correlation is weaker with the measured force deviating from the simulation results. This is partly attributed to poorer alignment of the insert within the C-channel in the Instron test as the insert emerges from the channel and the overlap region decreases. A better correlation can be achieved using a non-constant friction coefficient model in the simulation, where the coefficient is increased beyond the unstable equilibrium state.

Based on the difference in snap-through force seen in Fig. 9 for the two mechanisms, it can be expected that in a rotor test one of the inserts will extend first and the other one will follow at an increased RPM when the increased centrifugal force is large enough for the second mechanism to snap-through. Introducing friction force on the right hand side of Eq. 7, the dynamic simulation indicates an expected difference of 42 RPM between deployments of the two inserts (Fig. 10). A first rotor test was conducted and using the high-speed camera this event of extension on one side occurring before the other was captured, as shown in still frame Fig. 11. The asynchronous extension results in a highly imbalanced rotor, and power to the motor was immediately cut in the test.

To eliminate the possibility of asynchronous extension, a cable system was designed and introduced into the prototype that ensured synchronous extension of both inserts. Figure 12 shows the prototype rotor with the synchronizing cable mechanism. As seen in the figure a small pulley is introduced coincident to the mechanical stop on each blade section. Cable 1-2-3 connects the inboard ends of the two inserts going around the pulley on the right

blade (at point 2), and cable 3-4-1 connects the inboard ends of the two inserts going around the pulley on the left blade (at point 4). If the section on the left blade starts to deploy first at a lower RPM, cable 1-2-3 (in red on Fig. 12b) is put in tension. This has the effect of holding back the insert on the left blade and preventing it from deploying, while simultaneously pulling forward on the insert on the right blade and assisting its deployment. During this process the cable 3-4-1 goes slack and plays no role, but if the section on the right was to deploy first the roles of the two cables would be reversed.

Denoting x_1 as the direction the leading blade travels and x_2 as the direction of motion for the lagging blade, the simulation model solves the governing equation simultaneously for each blade. If T_c is the cable tension, then the equation for the lagging blade is

$$m\ddot{x}_2 + k\big(x_2 - L_0 sin(\theta_0)\big) - \frac{k\big(x_2 - L_0 sin(\theta_0)\big)}{cos(\theta_0)\sqrt{\frac{\big(x_2 - L_0 sin(\theta_0)\big)^2}{\big(L_0 cos(\theta_0)\big)^2} + 1}} = F_{CF}(x_2) - F_{FR} + T_c \cos\theta_d \quad [15]$$

and that for the leading blade is

$$m\ddot{x}_1 + k\big(x_1 - L_0 sin(\theta_0)\big) - \frac{k\big(x_1 - L_0 sin(\theta_0)\big)}{cos(\theta_0)\sqrt{\frac{\big(x_1 - L_0 sin(\theta_0)\big)^2}{\big(L_0 cos(\theta_0)\big)^2} + 1}} = F_{CF}(x_1) - F_{FR} - T_c \cos\theta_r \quad [16]$$

The angles θ_d and θ_r are shown on Fig. 12b. The appropriate values of friction coefficient are used for the two blades, and the normal force is adjusted to include the effect of cable tension in addition to the force exerted by the compression spring in the link. For the lagging blade,

$$F_{FR} = \mu(x_2)[k\Delta L_2 cos(\theta_0 - \theta_2) - T_c \sin(\theta_d)] \quad [17]$$

and for the leading blade,

$$F_{FR} = \mu(x_1)[k\Delta L_1 cos(\theta_0 - \theta_1) - T_c \sin(\theta_r)] \quad [18]$$

The instantaneous compression in the spring is calculated as

$$\Delta L_{1,2} = L_0 - \frac{L_0 cos\theta_0}{cos\Big(\text{atan}\Big(\frac{L_0 sin\theta_0 - x_{1,2}}{L_0 cos\theta_0}\Big)\Big)} \quad [19]$$

Where the instantaneous link angle is

$$\theta_{1,2} = \theta_0 - \text{acos}\left(\frac{L_0 cos\theta_0}{L_0 - \Delta L_{1,2}}\right) \quad [20]$$

If k_c is the axial stiffness of the cable, and ΔL_c is the extension in the cable, the cable tension is calculated as

$$T_c = k_c \cdot \Delta L_c(x_1, x_2) \quad [21]$$

The extension in the cable is calculated using

$$\Delta L_c = L_c(x_1, x_2) - L_{c0} \quad [22]$$

where the cable initial length, L_{c0}, and instantaneous length, $L_c(x_1, x_2)$, during deformation, are calculated using Fig. 13, as

$$L_{c0} = \sqrt{\big(\delta_p - \delta_1\big)^2 + h_p^2 - r_p^2} + r_p\left(\frac{\theta_w}{2\pi}\right) + \sqrt{\big(\delta_p + \delta_1\big)^2 + \big(L_0 cos\theta_0 - h_p\big)^2 - r_p^2} \quad [23]$$

$$\theta_w(x_1,x_2)=2\pi-\left[\cos^{-1}\left(\frac{r_p}{\sqrt{\left(\delta_p-\delta_1\right)^2+h_p^2}}\right)+\cos^{-1}\left(\frac{r_p}{\sqrt{\left(\delta_p+\delta_1\right)^2+\left(L_0cos\theta_0-h_p\right)^2}}\right)+\cos^{-1}\left(\frac{\left(\delta_p+\delta_1\right)\left(\delta_p-\delta_1\right)+\left(L_0cos\theta_0-h_p\right)h_p}{\sqrt{\left(\delta_p+\delta_1\right)^2+\left(L_0cos\theta_0-h_p\right)^2}\cdot\sqrt{\left(\delta_p-\delta_1\right)^2+h_p^2}}\right)\right] \quad [24]$$

$$L_c(x_1,x_2)=\sqrt{\left(\delta_p-\delta_1-x_2\right)^2+h_p^2-r_p^2}+r_p\theta_w(x_1,x_2)+\sqrt{\left(\delta_p+\delta_1+x_1\right)^2+\left(L_0cos\theta_0-h_p\right)^2-r_p^2} \quad [25]$$

$$\theta_w(x_1,x_2)=2\pi-\left[\cos^{-1}\left(\frac{r_p}{\sqrt{\left(\delta_p-\delta_1-x_2\right)^2+h_p^2}}\right)+\cos^{-1}\left(\frac{r_p}{\sqrt{\left(\delta_p+\delta_1+x_1\right)^2+\left(L_0cos\theta_0-h_p\right)^2}}\right)+\cos^{-1}\left(\frac{\left(\delta_p+\delta_1+x_1\right)\left(\delta_p-\delta_1-x_2\right)+\left(L_0cos\theta_0-h_p\right)h_p}{\sqrt{\left(\delta_p+\delta_1+x_1\right)^2+\left(L_0cos\theta_0-h_p\right)^2}\cdot\sqrt{\left(\delta_p-\delta_1-x_2\right)^2+h_p^2}}\right)\right] \quad [26]$$

Using the simulation model described above and solving for extension of both blades simultaneously, the blades were observed to deploy synchronously, as seen in Fig. 14. Figure 15 shows the strain in the two cables as a function of extension. While one of the cables goes slack (negative $\Delta L_c/L_{c0}$, the other is in tension and produces the synchronized extension of the two blades seen in Fig. 14). The maximum tensile strain in the cable for the current configuration is seen to be 6E-4.

VI. Synchronous Extension Test

With the prototype refitted with the cable and pulley mechanisms to ensure synchronous extension another rotor test was carried out. The motor turn on RPM was 750 RPM, and the rotational speed was ramped up at 450 RPM/sec. With a predicted snap-through RPM of around 950, this ensured that the snap-through event and the extension of the rotor would be captured by the high-speed camera recording for 1 second. Using the frames from the high-speed camera, both the extension of the blade as well as the rotor RPM could be calculated. Figure 16 shows the experimentally measured extension versus RPM data, from several tests. Also included on the figure are simulation results for synchronous extension corresponding to a 450 RPM/sec ramp. The simulation results are seen to correlate very well with the high-speed camera data, with snap-through and extension occurring at around 950 RPM.

Figure 17 shows frames from the high-speed camera, and snap-through can be seen to be occurring over about quarter revolution (or 0.015 sec at 950 RPM). Importantly, both blades are seen to be extending in a synchronous manner. Figure 18 shows RPM readings from the Hall Effect sensor. When snap-through occurs, the increase in rotor inertia leads to an instantaneous reduction in rotor RPM. However, the RPM governor compensates and the RPM is quickly restored. The instantaneous reduction in RPM, as captured by the Hall effect sensor between 920 and 950 RPM (in 4 separate runs), corroborates the data obtained from the high-speed camera (presented in Fig. 17). Although not presented, it should be noted that the high-speed camera too recorded an instantaneous dip in RPM, followed by a quick recovery, when snap-through occurred.

VII. Summary and Concluding Remarks

This paper presents the concept of a span morphing blade for rotary-wing micro-aerial vehicle applications. The blades use a bi-stable mechanism that snaps-through when the RPM and centrifugal force increase beyond a critical value. The snap-through of the bi-stable mechanism results in rotor span extension when inserts connected to it and contained within the blade are deployed. The design and analysis of such a mechanism was presented in detail, and

a prototype was fabricated capable of span increase from 139 mm to 197 mm. Due to dissimilarity in friction between the two blades, one of the blades was predicted to extended earlier (about 40 RPM lower) than the other, and rotor test results verified this asynchronous extension.

To avoid imbalance problems associated with asynchronous extension of the two blades, a cable-pulley mechanism was designed and introduced into the prototype, and the simulation model was updated to account for it. The analytical model predicted that the cable-pulley mechanism would ensure synchronous extension of the two blades, with maximum tensile strains in the cable of 6E-4.

A second rotor test was conducted with the cable-pulley mechanism installed, and blade extension measurements were obtained using high-speed camera footage. RPM measurements were obtained from both high-speed camera data as well as from a Hall Effect sensor on the rotor shaft. Rotor test results showed synchronous extension of the two blades at around 950 RPM. From the high-speed camera data it was observed that snap-through occurred over about a ¼ revolution, or about 0.015 sec. The simulation results of rotor extension versus RPM compared well with test data. An instantaneous drop in RPM due to increase in rotor inertia was noted when snap-through occurred, but the RPM governor quickly restored the rotor speed.

A second generation prototype with aerodynamic surfaces and an improved mechanism design (Fig. 19) is currently under fabrication, with plans for testing on the rotor stand.

Acknowledgements

The authors gratefully acknowledge funding of these research activities by the Air Force Office of Scientific Research (grant number FA9550-11-1-0159) with Dr. David Stargel as the program manager. The authors would also like to thank Prof. Yoav Peles in the Mechanical Engineering program at RPI for the use of the high-speed camera during the rotor tests.

References

1. Bohorquez, F., Samuel, P., Sirohi, J., Pines, D., Rudd, L., and Perel, R., "Design Analysis and Hover Performance of a Rotating Wing Micro Air Vehicle," *Journal of American Helicopter Society*, Vol. 48, (2), April 2003, pp. 80–90.
2. Pines, D. J., and Bohorquez, F., "Challenges Facing Future Micro-Air-Vehicle Development," *Journal of Aircraft*, Vol. 43, (2), March–April 2006, pp. 290–305.
3. Chopra, I., "Hovering Micro Air Vehicles: Challenges and Opportunities," Proceedings of the International Forum on Rotorcraft Multidisciplinary Technologies, Oct. 15-17, 2007, Seoul, Korea.
4. Hein, B. R., and Chopra, I., "Hover Performance of a Micro Air Vehicle: Rotors at Low Reynolds Number," *Journal of American Helicopter Society*, Vol. 52, (3), July 2007, pp. 254-262.
5. Ramasamy, M., Johnson, B., Leishman, J. G., "Understanding the Aerodynamic Efficiency of a Hovering Micro-Rotor," *J. of American Helicopter Society*, Vol. 53, (4), Oct. 2008, pp. 412–428.
6. Fradenburgh, E. A., "Application of a Variable Diameter Rotor System to Advanced VTOL Aircraft," *31st American Helicopter Society Forum*, Washington, D.C., May 13-15, 1975.
7. Fradenburgh, E. A., and Matuska, D. G., "Advancing Tiltrotor State-of-the-art with Variable Diameter Rotors," *48th American Helicopter Society Forum*, Washington D.C., June 3-5, 1992.
8. Prabhakar, F. Gandhi, J. Steiner and D. McLaughlin, "A Centrifugal Force Actuated Variable Span Morphing Helicopter Rotor," *63rd Annual AHS International Forum and Technology Display*, Virginia Beach, VA, May 1-3, 2007.
9. Mistry, M., and Gandhi, F., "Helicopter Performance Improvement with Variable Rotor Radius and RPM," *Journal of the American Helicopter Society*, **59**, 042010 (2014).
10. Pontecorvo, M., Barbarino, S., Murray, G., and Gandhi, F., "Bi-Stable Arches for Morphing Applications" *J. of Intelligent Material Systems and Structures*, Vol. 24, No. 3, Feb 2013, DOI: 10.1177/1045389X12457252.
11. Diaconu, C. G., Weaver, P. M., and Mattonni, F., "Solutions for Morphing Airfoil Sections Using Bistable Laminated Compositie Structures," AIAA Structural Dynamics and Materials Conference, 23–26 April 2007, Honolulu, Hawaii.
12. M. Schultz, "A Concept for Airfoil-like Active Bistable Twisting Structures," *Journal of Intelliget Material Systems and Structures*, 2008.

13. Johnson, T., Frecker, M., and Gandhi, F., "A Bistable Mechanisms for Chord Extension Morphing Rotors," *Proc. of the 2009 SPIE Conf. on Smart Structures and Materials*, San Diego, California, March 8-12, 2009.
14. Johnson, T., Gandhi, F., and Frecker, M.,"Modeling and Experimental Validation of a Bistable Mechanism for Chord Extension Morphing Rotors," *Proc. of the 2010 SPIE Conf. on Smart Structures and Materials*, San Diego, California, March 7-11, 2010.
15. Moser, P., Barbarino, S., and Gandhi, F., "Helicopter Rotor Blade Chord Extension Morphing using a Centrifugally Actuated von-Mises Truss," *Journal of Aircraft*, Vol. 51, No. 5 (2014), pp. 1422-1431. doi: 10.2514/1.C032299.
16. Von Mises, R., "Über die Stabilitätsprobleme der Elastizitätstheorie," *Zeitschrift für Angewandte Mathematik und Mechanik*, Vol. 3, No. 6, 1923, pp. 406-422.

Figures

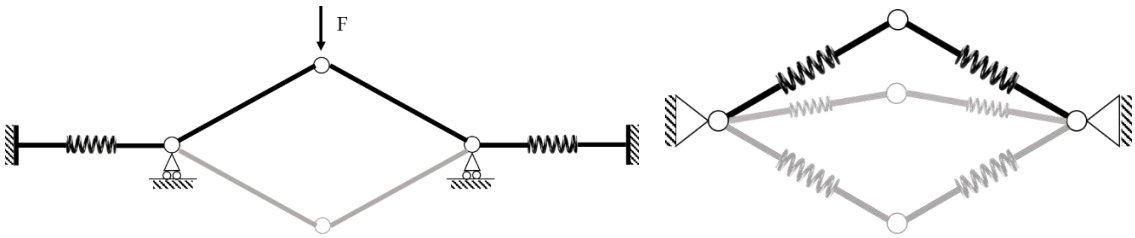

A B

Fig. 1: Von Mises Truss with (A) rigid links, and (B) variable length links showing the first and second stable equilibrium positions.

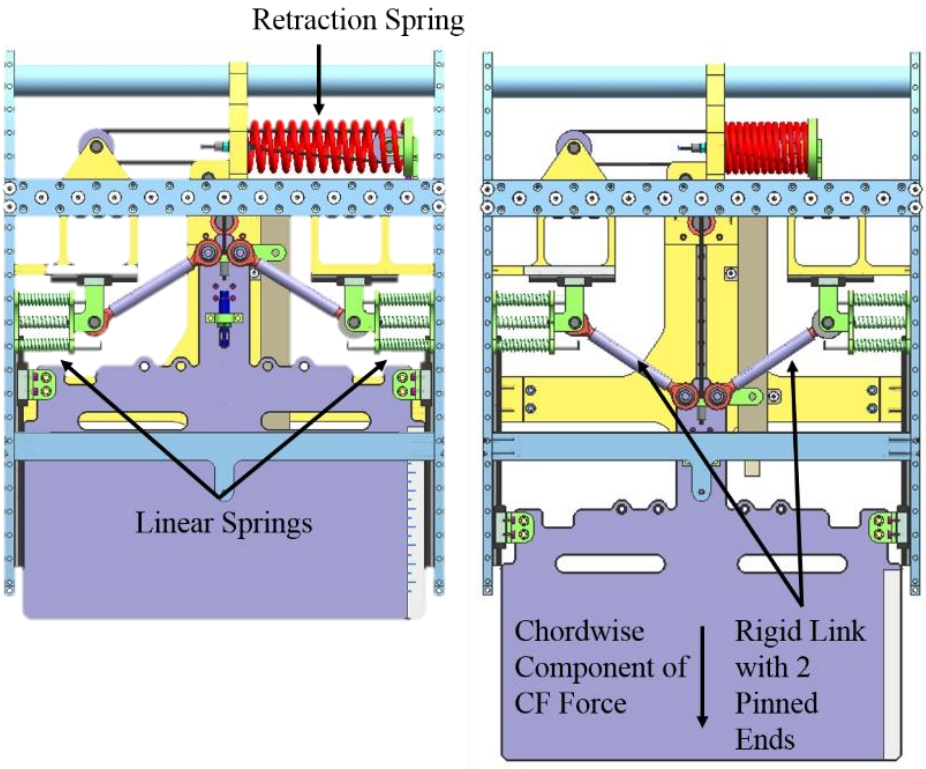

Fig. 2: Bi-stable chord morphing mechanism using Von Mises truss with rigid links (Ref. 15).

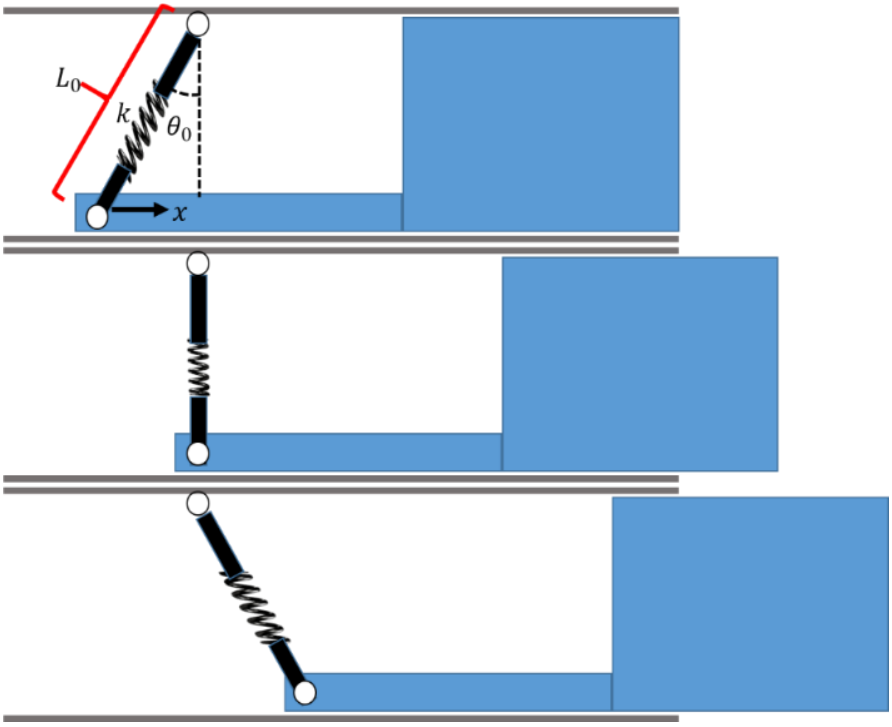

Fig.3: Schematic of bi-stable span morphing mechanism with half VMT.

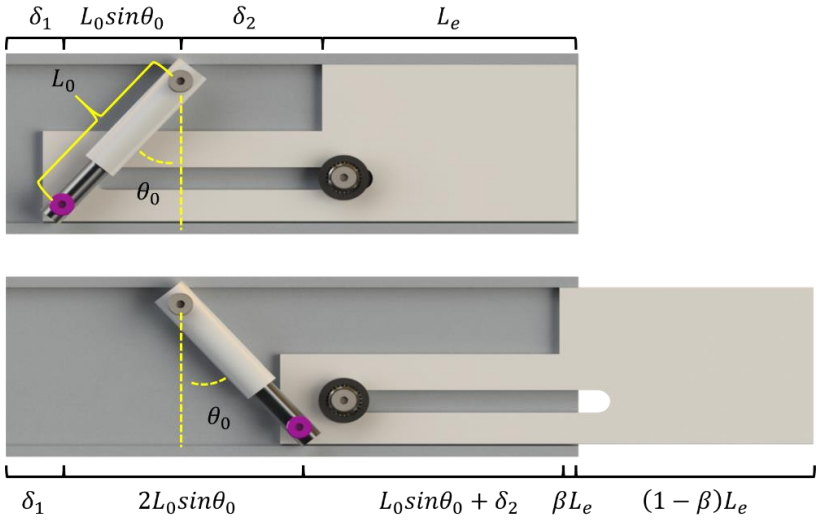

(A)

(B)

Fig. 4: Prototype rotor schematic with dimensions specified to describe the (A) retracted and (B) extended configurations.

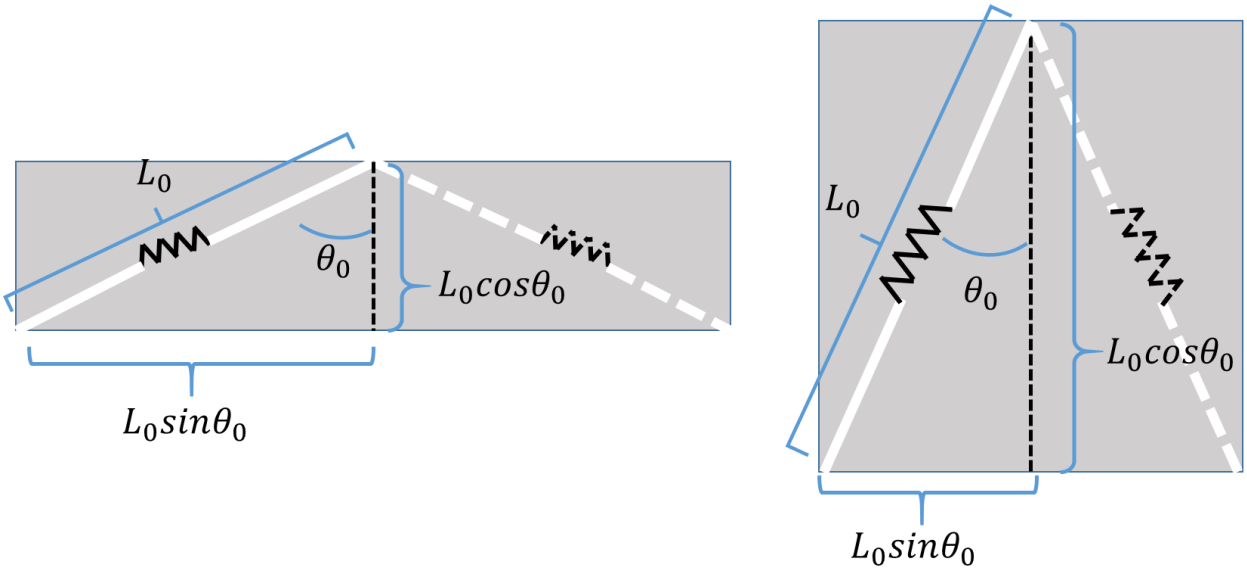

(A) (B)

Fig. 5: Relation of bi-stable mechanism stroke length to (A) internal spring strain and (B) channel width.

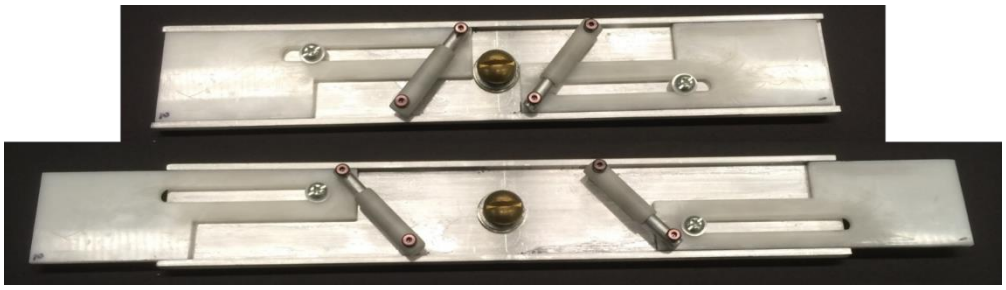

(A)

(B)

Fig. 6: Prototype rotor with inserts in the (A) retracted and (B) extended configuration.

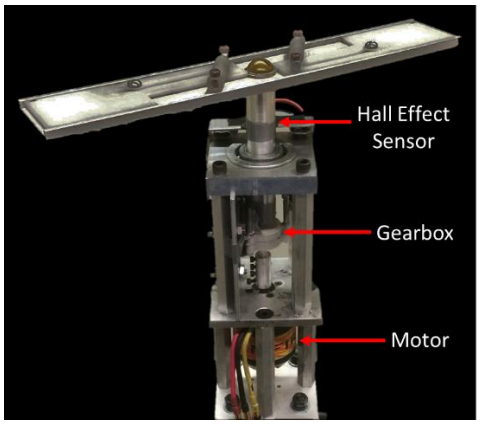

Fig. 7: Rotor test stand with motor, gearbox, RPM sensor, and prototype in compact configuration.

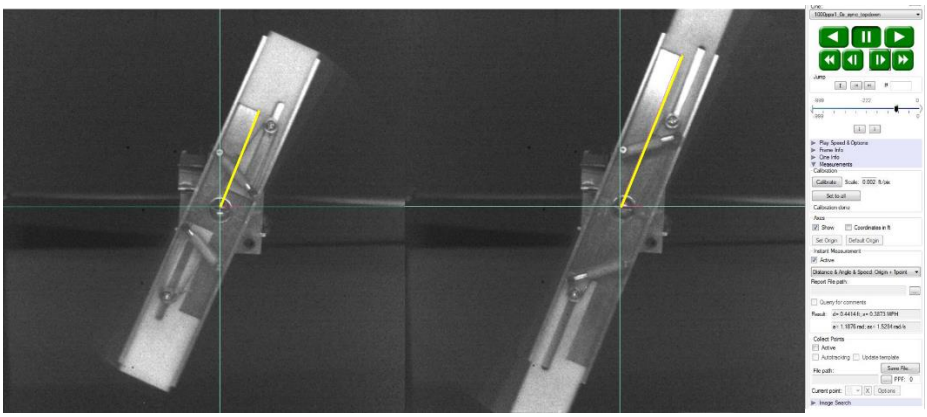

Fig. 8: Span extension measurements from position of insert in specific frames.

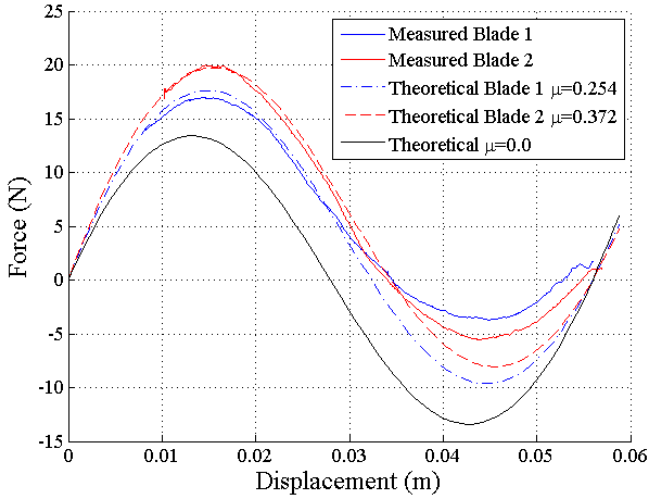

Fig. 9: Quasi-static force versus displacement behavior of the bi-stable mechanisms under displacement input.

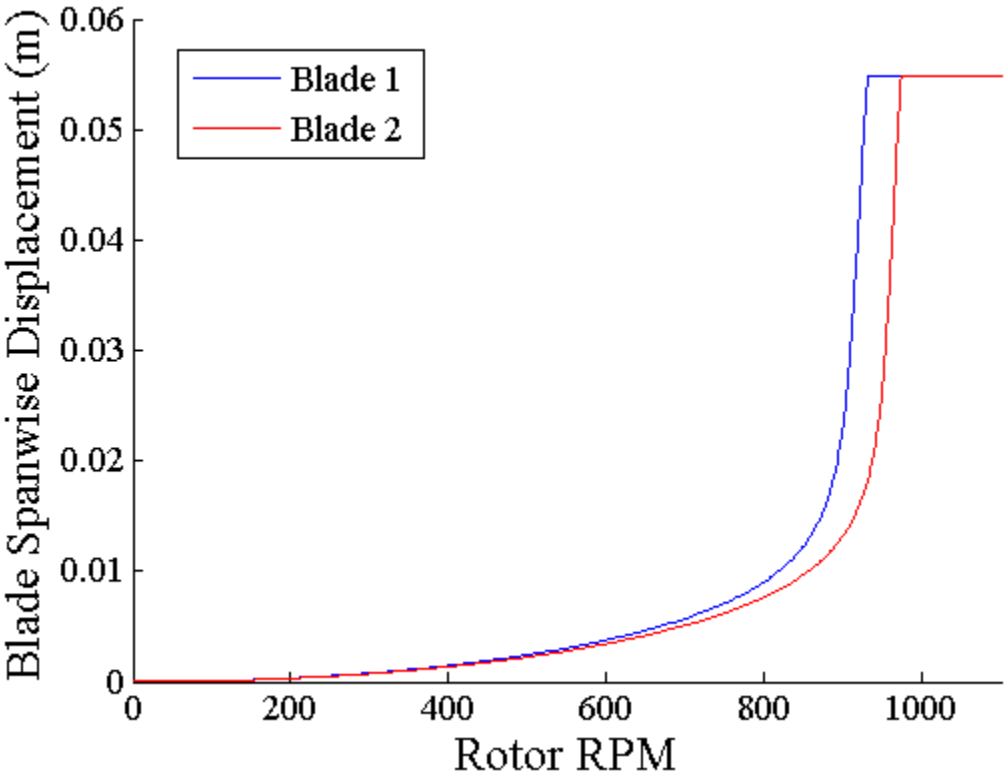

Fig. 10: Predicted extension of the two "blades" as a function of rotor RPM.

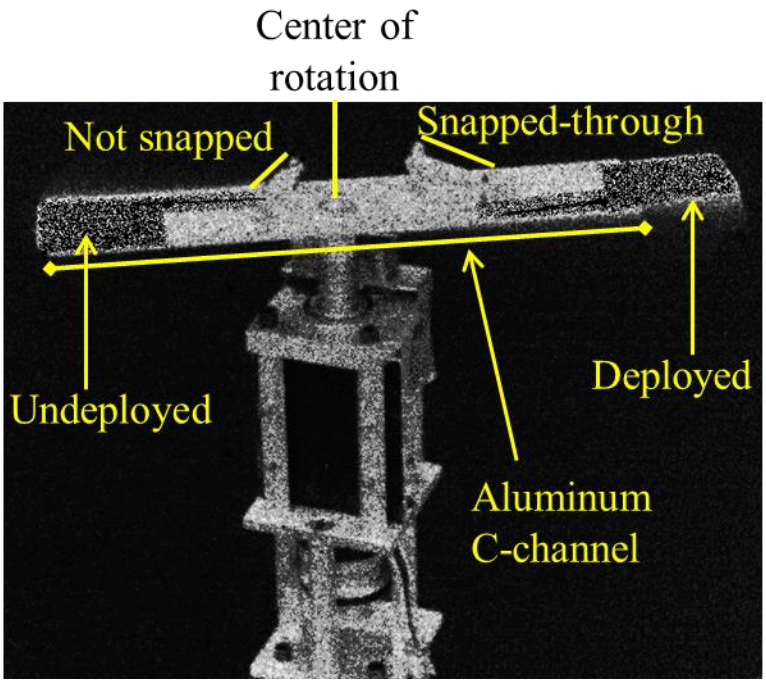

Fig. 11: High speed camera footage capturing asynchronous deployment.

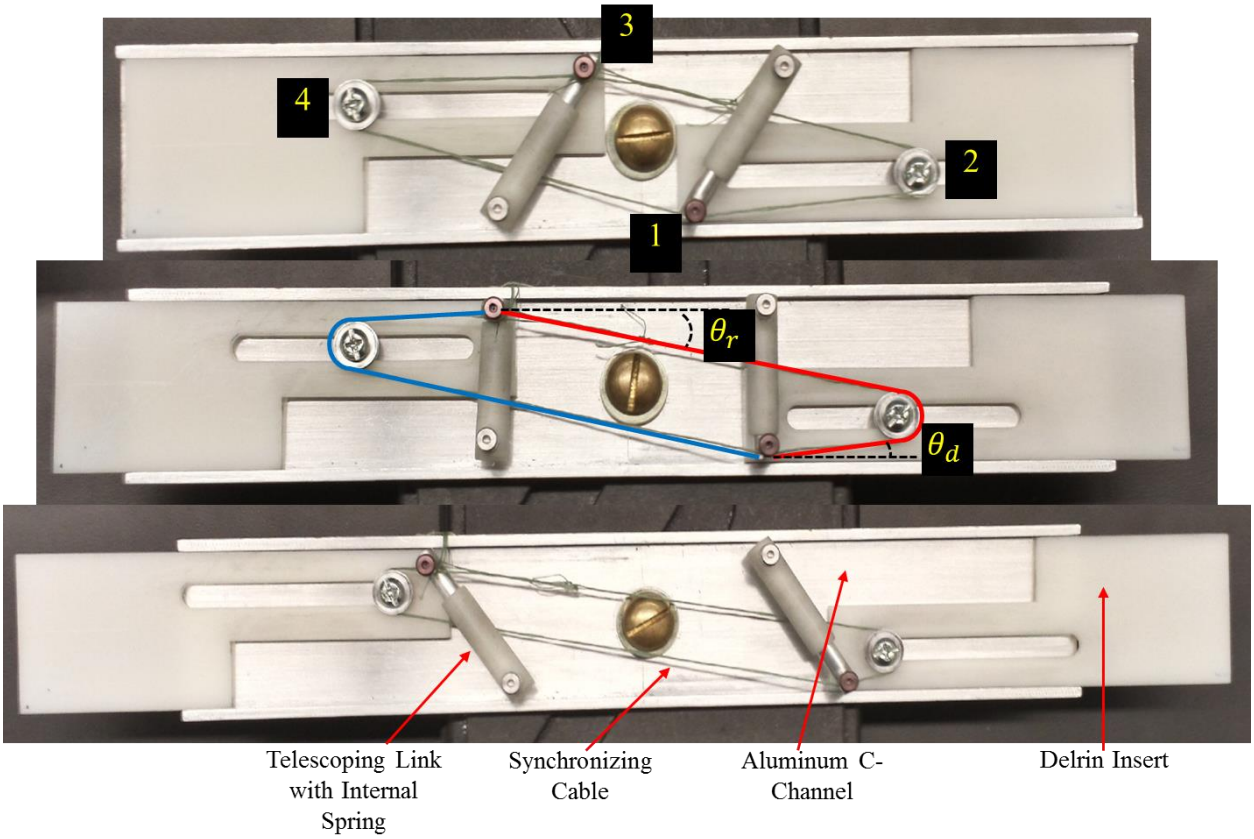

Fig. 12: Prototype with synchronizing cable in (a) retracted, (b) intermediate, and (c) extended configurations.

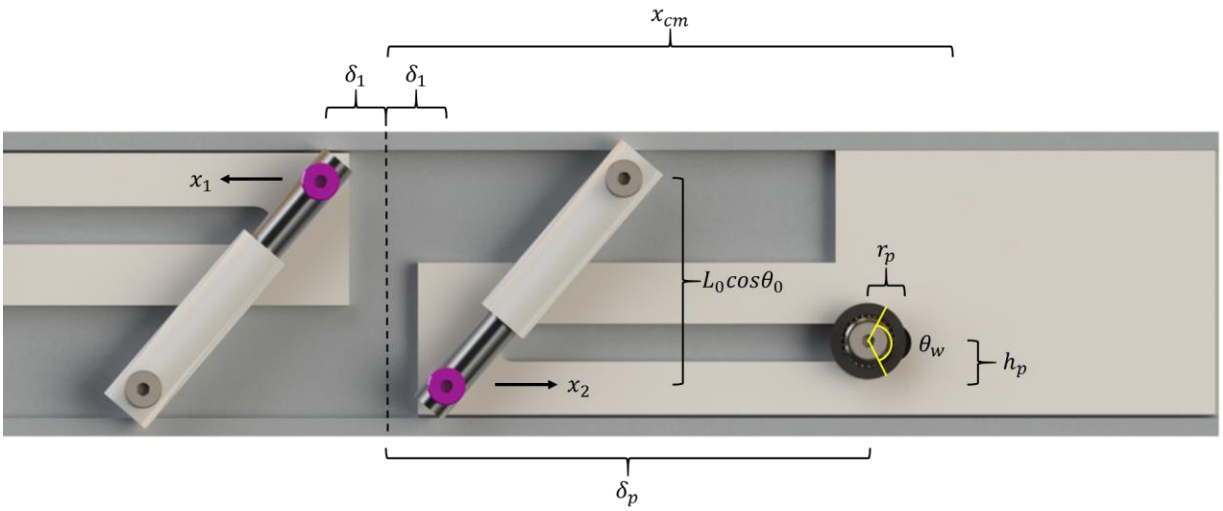

Fig. 13: Prototype rotor schematic with dimensions specified to calculate synchronizing cable length.

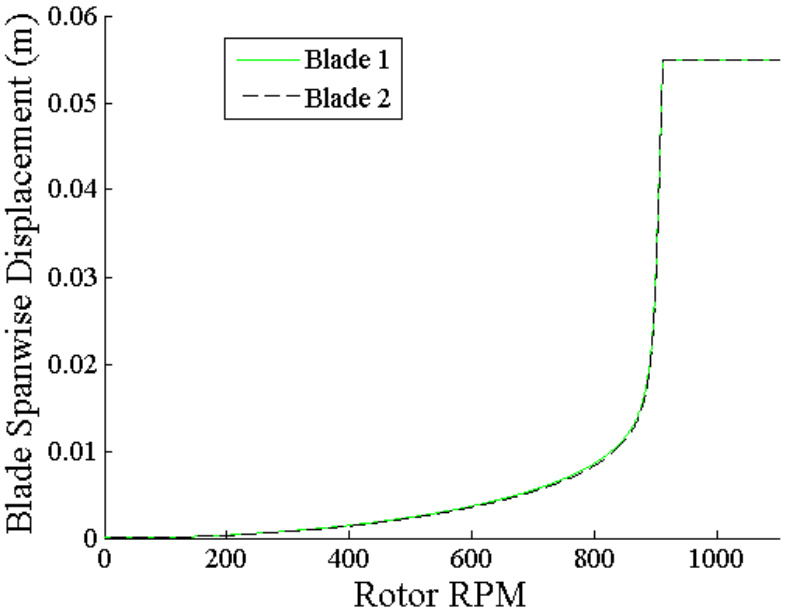

Fig. 14: Model prediction of synchronous extension of the two "blades" as a function of rotor RPM.

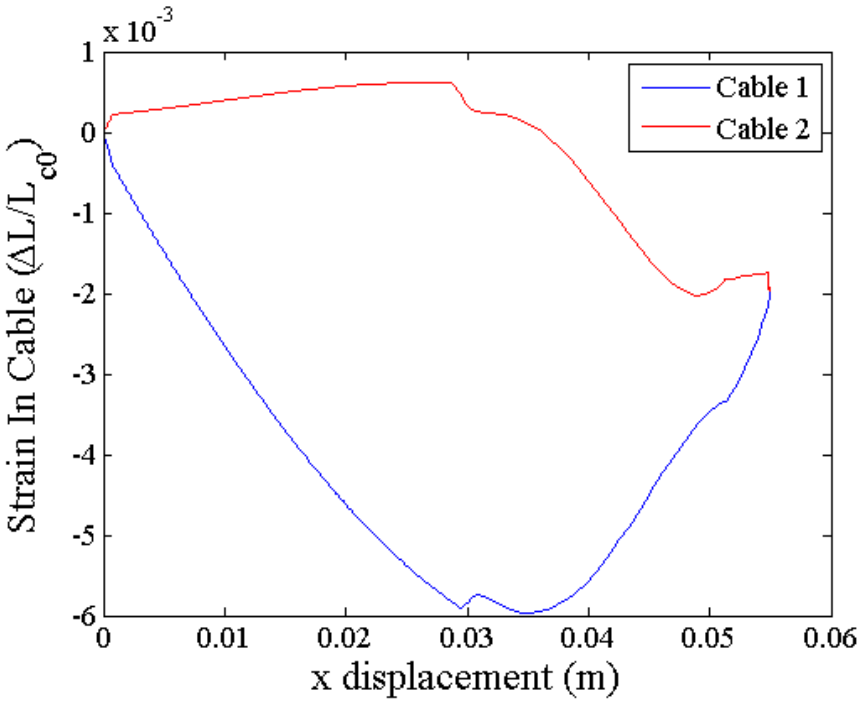

Fig. 15: Strain in the cables, as a function of blade extension.

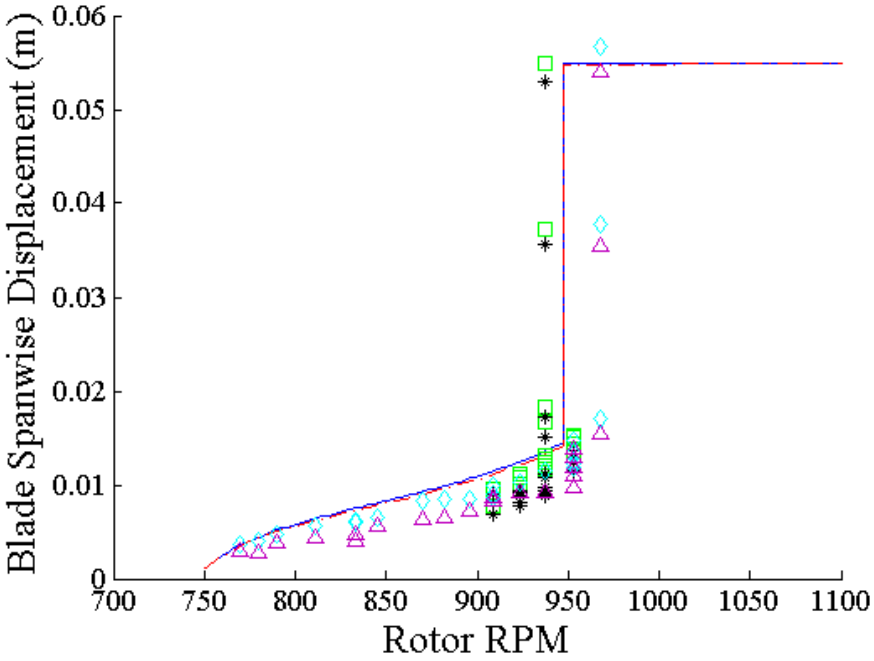

Fig. 16: High speed camera measurements of extension versus RPM, compared with simulation results.

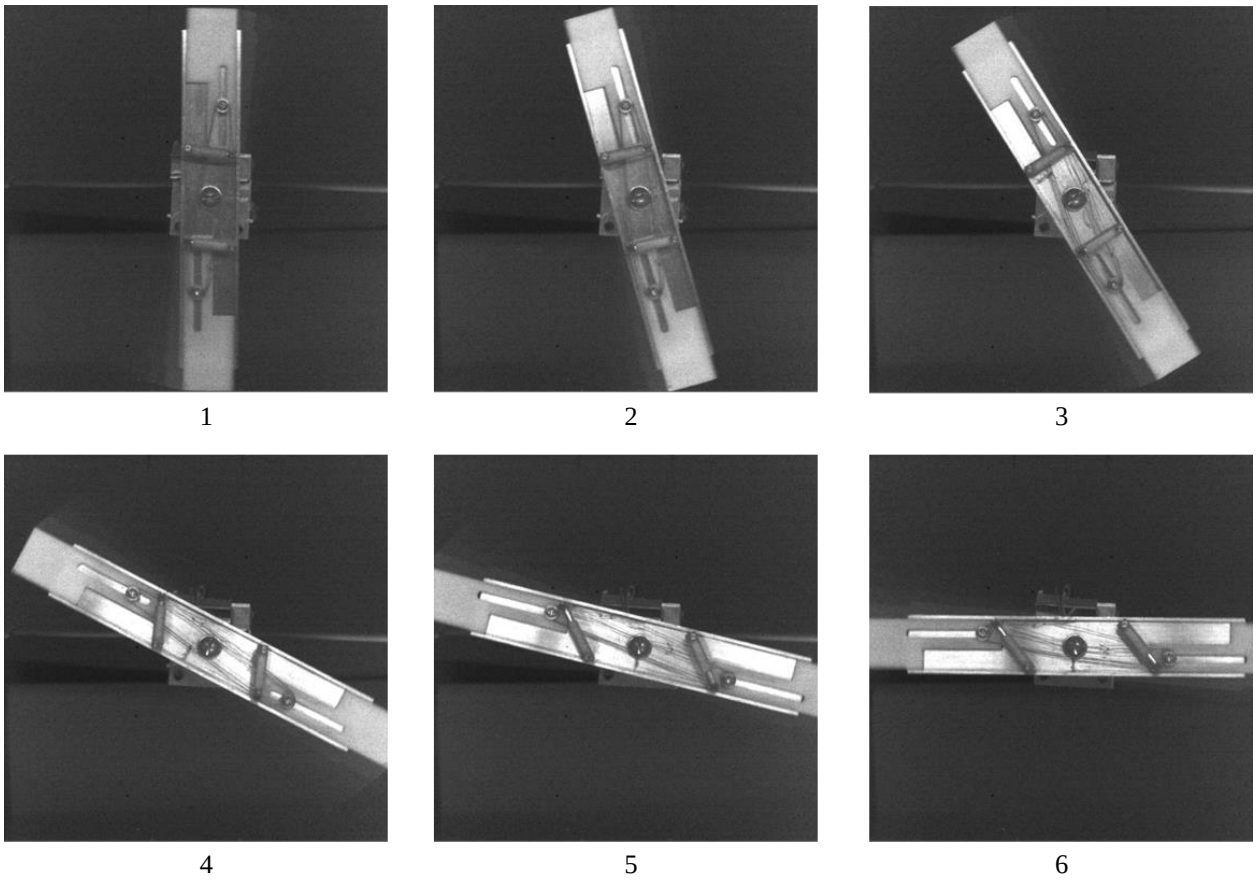

Fig. 17: Images of high-speed camera frames showing synchronous extension occurring over a ¼ revolution.

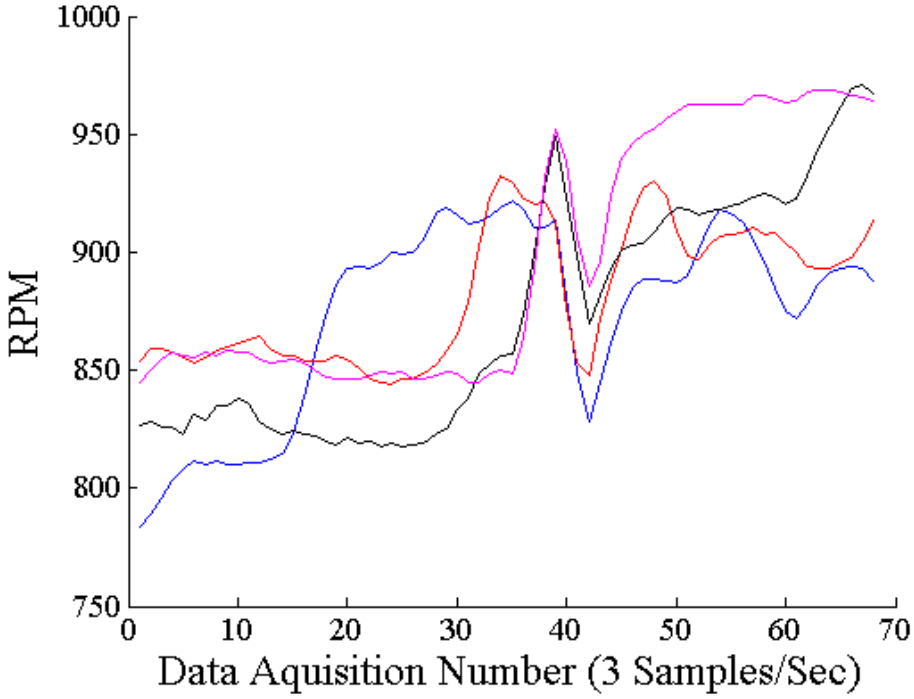

Fig. 18: Hall Effect sensor RPM data showing instantaneous change at snap-through.

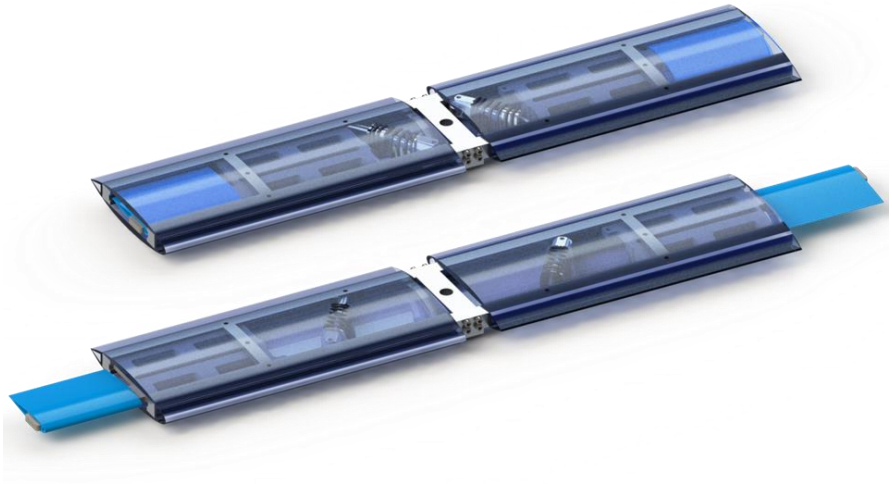

Fig. 19: Generation two span morphing rotor with aerodynamic surfaces